symmetry

MDPI

Article

Strong-Field Interaction of Molecules with Linearly Polarized Light: Pathway to Circularly Polarized Harmonic Generation

Shushan Zhou [1], Hao Wang [1], Nan Xu [1], Dan Wu [2,*] and Muhong Hu [1,*]

[1] School of Physics and Electronic Technology, Liaoning Normal University, Dalian 116029, China; zhoushushan@lnnu.edu.cn (S.Z.); 18018950396@163.com (H.W.); 13390283718@163.com (N.X.)
[2] College of Science, Jilin University of Chemical Technology, Jilin 132002, China
* Correspondence: wudan@jlict.edu.cn (D.W.); humuhong@163.com (M.H.)

Abstract

In recent years, the generation of circularly polarized attosecond pulses has garnered significant attention due to their potential applications in ultrafast spectroscopy and, notably, in chiral-sensitive molecular detection. The traditional methods for generating such pulses often involve complex laser configurations or specially engineered targets, limiting their experimental feasibility. In this study, we present a streamlined and effective approach to producing circularly polarized attosecond pulses by employing a linearly polarized laser field in conjunction with a stereosymmetric linear molecule, 1-butyne (C_4H_6). The generation of high-order harmonics by this molecular system reveals a distinct plateau in the perpendicular polarization component, which facilitates the generation of isolated attosecond pulses with circular polarization. Through a detailed analysis of the time-dependent charge density dynamics across atomic sites, we identify the atoms primarily responsible for the emission of circularly polarized harmonics in the plane orthogonal to the driving field. Moreover, we explore the role of multi-orbital contributions in shaping the polarization properties of the harmonic spectra. Our findings underscore the importance of molecular symmetry and the electronic structure in tailoring the harmonic polarization, and they demonstrate a viable pathway for using circularly polarized attosecond pulses to probe molecular chirality. This method offers a balance between simplicity and performance, opening new avenues for practical applications in chiral recognition and ultrafast stereochemical analysis.

Keywords: high-order harmonic generation; molecular alignment; circularly polarized attosecond pulses; time-dependent density functional theory

Academic Editor: Stefano Profumo

Received: 24 May 2025
Revised: 6 August 2025
Accepted: 12 August 2025
Published: 15 August 2025

Citation: Zhou, S.; Wang, H.; Xu, N.; Wu, D.; Hu, M. Strong-Field Interaction of Molecules with Linearly Polarized Light: Pathway to Circularly Polarized Harmonic Generation. *Symmetry* **2025**, *17*, 1329. https://doi.org/10.3390/sym17081329

1. Introduction

Owing to continuous efforts by researchers worldwide, laser research has rapidly advanced and become a central topic in modern physics. Notable achievements include the enhancement of laser intensities [1–7] and the development of ultrafast lasers capable of generating attosecond pulses (1 as $= 10^{-18}$ s) [8,9]. This technological breakthrough has opened new frontiers in fundamental scientific investigations, particularly in quantum dynamics and light–matter interactions. Of particular significance, the intricate interplay between intense laser fields and atomic/molecular systems has emerged as a pivotal research domain, offering unprecedented opportunities to probe electron dynamics at their natural timescales and manipulate quantum states with light-wave precision.

When intense laser fields interact with atoms or molecules, high-harmonic generation (HHG) occurs, producing radiation at integer multiples of the laser's frequency [10–12]. Experimental studies show that the harmonic intensity initially drops rapidly with increasing order and then forms a nearly flat "plateau" region before falling off sharply at the "cutoff" [13,14]. The plateau, which spans a broad spectral range, is crucial for generating coherent EUV and soft X-ray radiation [15], enabling applications in ultrafast spectroscopy and attosecond science.

To explain the unique spectral features of HHG, Corkum and colleagues proposed the semi-classical three-step model, which remains a cornerstone in strong-field physics [16]. In this model, the electrons first undergo ionization, primarily via tunneling when the laser's intensity is high and the frequency is low [17,18]. Next, the freed electrons are accelerated by the oscillating laser field, with some returning to the ion core. Upon recombination, their kinetic energy is released as high-energy photons, producing high-order harmonics. This model not only explains the formation of the spectral plateau and cutoff but also bridges classical electron trajectories with quantum recombination, offering clear physical insights and predictive power for attosecond science [19]. Although the three-step model provides a general framework for understanding HHG, it does not fully capture the complex dynamics of the molecules, such as the influence of the multi-center structure and electronic orbital shape. Therefore, more refined models, such as the Lewenstein model [20] and its adaptations for molecular systems, are essential for describing HHG by molecules more accurately. Specifically, Lewenstein et al. solved the time-dependent Schrödinger equation based on three key assumptions: (1) only the ground state contributes significantly to the electronic wave packet, while the contributions from other bound states are negligible; (2) the ground state is lossless; and (3) the electron in the continuum can be treated as a free particle driven solely by the laser field, with negligible influence from the atomic potential. According to this model, the electron is first ionized by the strong laser field into the continuum, then propagates under the laser field influence, and finally recombines with the parent ion via a dipole transition. The harmonic dipole moment arises from the coherent sum of different quantum paths corresponding to ionization, propagation, and recombination, consistent with the physical picture described by the three-step model.

Extensive research has revealed that attosecond pulses can be precisely manipulated by modulating the polarization of the laser, rendering this area an ever more prominent and sought-after topic in the scientific community. Driven by the pursuit of obtaining circularly polarized attosecond pulses, scores of dedicated researchers have spared no effort and conducted a plethora of innovative attempts. Circular attosecond pulses can be successfully generated via two distinct strategies: modifying the characteristics of the laser field and substituting the target materials with different substances.

One effective strategy focuses on tailoring the laser field itself. Various configurations, including non-uniform fields, multi-beam setups, and polarization combinations, have been explored for generating circularly polarized attosecond pulses. These include methods utilizing circular spectral components from spatially varying fields [21], intersecting beams [22], and two-color circular drivers [23]. Further advances involve the use of three precisely tuned fields [24], orthogonal polarization combinations [25], and structured fields with rotating polarization and azimuthal phase gratings [26]. These schemes have not only enhanced the polarization control but have also pushed the spectral range into the vacuum-ultraviolet and soft X-ray regimes [27,28]. Additionally, theoretical investigations demonstrate that isolated circular pulses with controllable helicity can be achieved via polarization gating and proper alignment of the molecular targets [29]. Another complementary approach involves engineering the target medium. By employing specific molecular systems or mixed gases, the generation of circular attosecond pulses can be

facilitated even under conditions where harmonic generation is typically inefficient. Successful implementations include hybrid laser–molecule interactions [30], ring molecular structures [31], and relativistic laser interactions with magnetized plasma [32]. Moreover, schemes based on bichromatic fields interacting with gas mixtures have proven effective for producing near-circular or fully circular attosecond bursts [33,34]. While these approaches offer increased flexibility, they often come with challenges in experimental realization due to the complexity of the target preparation or the need for precise field control.

To address these challenges, we propose a simplified and efficient scheme that combines a linearly polarized laser with a structurally straightforward stereomolecular target, 1-butyne (C_4H_6). This linear molecule, characterized by terminal methyl groups, exhibits favorable symmetry for strong-field interactions. Our results demonstrate that circularly polarized attosecond pulses can be synthesized from the perpendicular component of the linearly polarized harmonic emission. In addition, we perform a detailed analysis of the time-dependent variations in the charge density around individual atomic sites within the molecule, revealing the specific atoms that contribute most to circular HHG emissions in the polarization plane. Furthermore, we explore the role of multiple molecular orbitals in the harmonic generation process, uncovering important multi-orbital effects. This study not only presents a feasible and efficient route for circular attosecond pulse generation but also provides deeper insight into the atomic-scale and orbital-level mechanisms involved in polarization-resolved HHG from polyatomic molecules.

2. Materials and Methods

To generate circularly polarized attosecond pulses, we adopted time-dependent density functional theory as the computational approach. Through a detailed analysis of molecular orbitals, we revealed the underlying mechanism of harmonic emission, which enabled the successful synthesis of circular attosecond pulses. As a powerful and widely applied tool, TDDFT has proven effective for investigating HHG in molecules subjected to intense laser fields [35,36].

According to the Runge–Gross theorem [37], for a many-electron system evolving from a fixed initial state, a unique correspondence between the time-dependent external potential and the resulting time-dependent electron density exists. In this study, spin polarization effects are not considered in the numerical simulations. The target molecule C_4H_6, which contains a methyl group at each end, can be regarded as a three-dimensional molecule and remains in a spin singlet state in its ground state. For comparison, we selected the linear molecule C_4H_2, which has a different structure but a similar molecular length (in the z-axis direction) to C_4H_6, and the much smaller C_2H_2 molecule. Both reference molecules also reside in spin singlet states in their ground states. Additionally, the Be atom was chosen as another reference target. In addition, to address the issue of degenerate molecular orbitals, we computed the high-order harmonic spectra for each degenerate orbital and took into account the contribution of each orbital to the overall harmonic emission. Under the length gauge and dipole approximation, the dynamics of electrons in a molecular system subjected to a linearly polarized laser field are governed by the time-dependent Kohn–Sham (KS) equations for the orbitals $\psi_i(\mathbf{r},t)$ (atomic units are used throughout):

$$i\frac{\partial}{\partial t}\psi_i(\mathbf{r},t) = \left[-\frac{1}{2}\nabla^2 + V_{\mathrm{KS}}[\rho(\mathbf{r},t)]\right]\psi_i(\mathbf{r},t), \quad i = 1,\cdots N. \tag{1}$$

Here, i is the orbital index, N is the number of Kohn–Sham orbitals, and $\rho(\mathbf{r},t)$ is the time-dependent electron density, $\rho(\mathbf{r},t) = 2\sum_{j=1}^{N}\left|\psi_j(\mathbf{r},t)\right|^2$.

The Kohn–Sham potential $V_{\mathrm{KS}}[\rho(\mathbf{r},t)]$, a function of $\rho(\mathbf{r},t)$, is defined as

$$V_{\mathrm{KS}}[\rho(\mathbf{r},t)] = V_{\mathrm{xc}}[\rho(\mathbf{r},t)] + V_{\mathrm{H}}[\rho(\mathbf{r},t)] + V_{\mathrm{ne}}(\mathbf{r}) + V_{\mathrm{laser}}(\mathbf{r},t) \tag{2}$$

The first term, $V_{\mathrm{xc}}[\rho(\mathbf{r},t)]$, denotes the exchange-correlation potential, which captures the nonperturbative many-body interactions and is treated using the Perdew–Burke–Ernzerhof (PBE) functional within the generalized gradient approximation (GGA) [38]. The second term, $V_{\mathrm{H}}[\rho(\mathbf{r},t)]$, represents the Hartree potential, accounting for classical electron–electron repulsion. The third term, $V_{\mathrm{ne}}(\mathbf{r})$, describes the electron–nucleus interaction, modeled via norm-conserving Troullier–Martins pseudopotentials [39] parameterized in the Kleinman–Bylander form [40]. Lastly, $V_{\mathrm{laser}}(\mathbf{r},t)$ corresponds to the interaction with the external laser field, expressed as $V_{\mathrm{laser}}(\mathbf{r},t) = \mathbf{r}\cdot\mathbf{E}(t)$, where $\mathbf{E}(t)$ is the time-dependent electric field of the linearly polarized laser.

The time-dependent Kohn–Sham orbital wavefunctions were evolved in real time on a spatial grid. To ensure numerical stability and maintain time-reversal symmetry during propagation, we adopted the approximated enforced time-reversal symmetry (AETRS) scheme [41], with a time step of 0.00192 fs.

While Equations (1) and (2) provide the theoretical foundation, subsequent Equations (3) to (8) describe the physical quantities that are directly evaluated in our numerical calculations. By solving Equations (1) and (2), we obtain the time-dependent electron density. Since these physical quantities are functionals of the electron density, we can extract important information about the system under investigation. We use the open-source software Octopus (version 9.2) [35,36,42–44] for real-time and real-space numerical simulations, employing the DFT method for ground-state calculations and the TDDFT method for time-dependent calculations. Unlike traditional quantum chemistry packages, Octopus does not utilize an orbital basis set. Instead, the time-dependent Kohn–Sham equations are solved directly on a uniform spatial grid, ensuring high accuracy and full flexibility in representing the electronic wavefunctions.

To suppress unphysical reflections of the electron wave packet at the boundaries, a complex absorbing potential (CAP) [45] was applied near the edges of the simulation box:

$$V_{\mathrm{absorb}}(\mathrm{r}) = \begin{cases} 0, & 0 < \mathrm{r} < \mathrm{r_{max}} \\ i\eta \sin^2\left[\frac{(\mathrm{r}-\mathrm{r_{max}})\pi}{2L}\right], & \mathrm{r_{max}} < \mathrm{r} < \mathrm{r_{max}} + \mathrm{L} \end{cases} \tag{3}$$

Here, the absorbing potential is characterized by a width of $L = 5.29$ Å and a strength parameter $\eta = -0.42$ Å.

The corresponding high-harmonic spectrum is calculated from the time-dependent dipole acceleration $\mathbf{a}(t)$ [46]:

$$H(\omega) = \left| \int \mathbf{a}(t) e^{-i\omega t} dt \right|^2 \tag{4}$$

where $\mathbf{a}(t) = -\int \rho(\mathbf{r},t)\nabla H_{\mathrm{KS}} d^3\mathbf{r}, \quad H_{\mathrm{KS}} = -\frac{1}{2}\nabla^2 + V_{\mathrm{KS}}[\rho(\mathbf{r},t)]$.

The components of the $\mathbf{a}(t)$ in the y and z directions are defined as

$$\mathbf{a}_{\mathrm{p}}(t) = -\int d^3\mathbf{r}\rho(\mathbf{r},t)\nabla\{V_H[\rho(\mathbf{r},t)] + V_{\mathrm{ne}}(\mathbf{r}) + V_{\mathrm{xc}}[\rho(\mathbf{r},t)]\} - N\cdot\mathbf{E}_{\mathrm{p}}(t) \quad \mathrm{p} = \mathrm{y},\mathrm{z} \tag{5}$$

where y and z represent the laser polarization directions.

By performing a Fourier transform on $\mathbf{a}_{\mathrm{p}}(t)$, the following expression is obtained:

$$\tilde{\mathbf{a}}_{\mathrm{p}}(\omega) = \int \mathbf{a}_{\mathrm{p}}(t)\mathrm{e}^{-i\omega t} dt \quad \mathrm{p} = \mathrm{y},\mathrm{z} \tag{6}$$

The harmonic ellipticity [47] is subsequently determined:

$$\varepsilon = \frac{|\tilde{\mathbf{a}}_+| - |\tilde{\mathbf{a}}_-|}{|\tilde{\mathbf{a}}_+| + |\tilde{\mathbf{a}}_-|} \tag{7}$$

where $\tilde{\mathbf{a}}_\pm = \frac{1}{\sqrt{2}}\left(\tilde{\mathbf{a}}_y \pm i\tilde{\mathbf{a}}_z\right)$.

By selecting the coherent superposition of harmonics within a specific energy range, an attosecond pulse can be synthesized [48], with its intensity expressed as follows:

$$I(t) = \left| \int_q \tilde{\mathbf{a}}_q e^{iq\omega_0 t} \right|^2 \tag{8}$$

where q is the harmonic order.

3. Results and Discussion

3.1. High-Harmonic Generation of a C_4H_6 Molecule in a Linearly Polarized Laser Field

First, we simulated the high-harmonic generation of the C_4H_6 molecule in a linearly polarized laser field using the TDDFT. The resulting harmonic spectra are shown in Figure 1a. Octopus performs numerical simulations in real time and real space. In our calculation, the simulation box was set in Cartesian coordinates with dimensions of 105.80 Å, 52.90 Å, and 105.80 Å along the x, y, and z axes, respectively. The spatial grid spacing was 0.20 Å in all three directions. The molecular long axis was aligned along the z-axis, and the ball-and-stick model of the molecule is shown in the inset of Figure 1. To investigate the orientation-dependent features of high-order harmonic generation, it is essential to align the molecular axis relative to the direction of laser polarization. In our study, the molecular long axis is assumed to be aligned along the z-axis. Molecular alignment is typically achieved using a preceding weak laser pulse that creates a rotational wave packet, aligning the molecules transiently before the arrival of the driving laser. Although perfect alignment is not experimentally achievable, a high degree of alignment is sufficient to reveal key physical effects. The influence of partial misalignment is expected to slightly broaden or weaken the signal but does not qualitatively affect the main conclusions. Moreover, the femtosecond duration of the driving pulse is much shorter than the typical rotational periods (several picoseconds) of molecules like C_4H_6, ensuring that the alignment remains largely unchanged during the HHG process. The yellow double arrow represents the polarization direction of the incident laser field, which is along the x-axis, with a wavelength of 800 nm, a peak field amplitude of 0.31×10^9 V/cm, and a trapezoidal envelope: the total duration is 15.84 fs (1 s = 10^{15} fs), the rising and falling edges span one optical cycle each, and the plateau lasts for four optical cycles.

In Figure 1a, the black curve represents the total harmonic spectrum of the molecule, while the red, blue, and green curves correspond to the harmonic components in the x, y, and z directions, respectively. It is evident that the harmonic spectrum in the x direction closely overlaps with the total harmonic spectrum, indicating that the HHG is mainly oriented along the x direction. This observation is consistent with our understanding of molecular HHG under a linearly polarized field. However, significant harmonic signals are also observed in the y and z directions. These spectra exhibit the typical features of HHG, including a rapid drop, a plateau, and a well-defined cutoff. Although the harmonic intensities in the y and z directions are approximately two orders of magnitude lower than that in the x direction, their presence is still meaningful. Notably, the comparable intensities in y and z suggest the possibility of synthesizing circularly polarized harmonics in the y-z plane, which is perpendicular to the incident laser field. This may offer potential applications in molecular chirality detection.

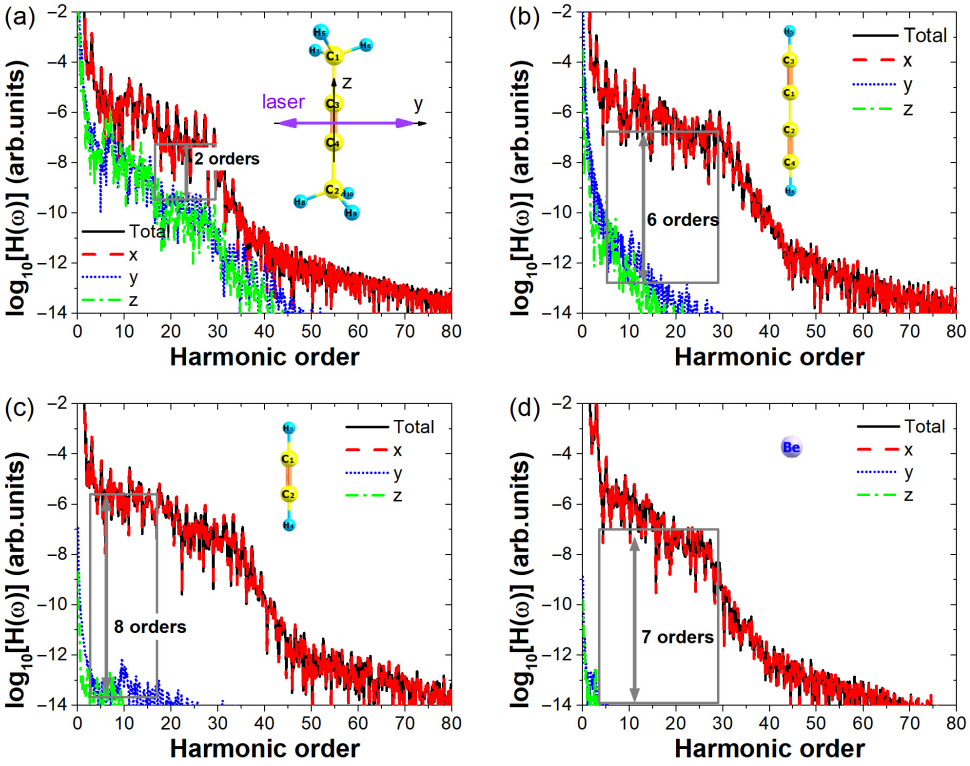

Figure 1. (**a**) The high-order harmonic spectrum of the C_4H_6 molecule. The black solid line represents the total harmonic yield, and the red, blue, and green curves represent the harmonic components along the x, y, and z directions, respectively. The inset shows the ball-and-stick model of the molecule, where the purple double arrow indicates the direction of polarization of the linearly polarized electric field. (**b**) The high-order harmonic spectrum of the C_4H_2 molecule. The inset shows the ball-and-stick model of the C_4H_2 molecule. (**c**) The high-order harmonic spectrum of the C_2H_2 molecule. The inset shows the ball-and-stick model of the C_2H_2 molecule. (**d**) The high-order harmonic spectrum of the Be atom. The inset shows the ball-and-stick model of the Be atom.

To verify this unique phenomenon, we selected three target species as references: the C_4H_2 molecule (with a length close to 5.89 Å), also known as diacetylene, is a linear carbon chain molecule with two hydrogen atoms at the ends. It differs structurally and electronically from C_4H_6, which is a conjugated diene with different bonding characteristics. We also used the C_2H_2 molecule (with a length close to 3.33 Å) and the Be atom. In this work, we define the molecular length as the size of the molecule along the z-axis. The length of C_4H_6 is 4.90 Å. The calculated ionization energies are 8.56 eV [49] for C_4H_6, 9.99 eV [50] for C_4H_2, 12.40 eV [51] for C_2H_2, and 9.56 eV [52] for the Be atom. The computational results for the ionization energies are in close agreement with the experimental data, confirming their reliability. Since the harmonic intensity is determined by both ionization and recombination probabilities and the molecules in question have different ionization potentials, we aimed to minimize the influence of these differences in our comparative analysis. To ensure that all molecules were studied under the same ionization regime, we kept the Keldysh parameter γ constant by adjusting the laser field's intensity for each case [53]. The Keldysh parameter is defined as $\gamma = \frac{\omega\sqrt{2I_p}}{E}$, where ω is the angular frequency of the laser, I_p is the ionization energy, and E is the electric field amplitude. For the C_4H_6 molecule, we used an electric field amplitude of 0.31×10^9 V/cm, which corresponded to a Keldysh parameter of $\gamma = 0.77$. Based on this value, the required field amplitudes were calculated for the other molecules: 0.33×10^9 V/cm for C_4H_2 (Figure 1b), 0.37×10^9 V/cm for C_2H_2 (Figure 1c),

and 0.32×10^9 V/cm for Be (Figure 1d). With these adjusted field amplitudes and all other laser parameters held constant, we simulated the high-order harmonic generation for the four molecules. The corresponding spectra are shown in Figure 1. Under the same laser parameters, all three reference targets exhibited harmonic spectra dominated by the x direction, while their harmonic intensities in the y or z directions were 6, 8, and 7 orders of magnitude weaker, respectively, than the total spectrum. This implies that they generate almost no harmonics in the y and z directions, forming a stark contrast to the behavior of C_4H_6.

To further confirm this phenomenon, we performed simulations of the HHG from the C_4H_6 molecule under various laser field parameters. The corresponding HHG spectra are shown in Figure 2. Figure 2a–c correspond to laser wavelengths of 600 nm, 1000 nm, and 1200 nm, respectively, while Figure 2d–f correspond to laser field amplitudes of 0.21×10^9 V/cm, 0.26×10^9 V/cm, and 0.36×10^9 V/cm, respectively. It can be clearly seen that as the wavelength increases, the cutoff of the harmonic spectrum gradually extends, with the cutoff harmonic order increasing from approximately the 15th to the 35th order. The plateau region also broadens, and significant harmonic emissions are consistently observed in the y and z directions. With an increase in the laser intensity, the cutoff harmonic order also increases significantly, from about the 15th to the 70th order. The harmonic spectra along the y and z directions exhibit the typical characteristics of a fast decay region, a plateau, and a cutoff. To understand the origin of the harmonic emissions in the y and z directions, we analyzed the time-dependent charge variation around the nuclei in the molecule. The results are presented in Figure 3.

To identify which atomic nuclei were primarily responsible for the HHG emissions in the y and z directions, we performed a time–frequency analysis of the HHG spectra in these two directions to determine the key emission times. For a clearer observation of the spectra, Figure 3a and 3d, respectively, reproduce the y and z direction harmonic spectra from Figure 1a. The plateau region of the spectra spans approximately from the 6th to the 27th harmonic order. Figure 3b and 3e present time–frequency maps of the HHG spectra for the y and z directions, respectively. In these plots, the horizontal axis denotes the emission time, the vertical axis indicates the harmonic order, and the color scale represents the intensity. From the maps, three main emission times for the y direction harmonics are identified, 7.20 fs, 9.84 fs, and 12.48 fs, as marked by dashed lines. For the z direction, the main emission times are 5.76 fs, 8.40 fs, and 11.04 fs, marked by solid black lines. After determining the key emission times, we plotted the time-dependent charge variation around different atomic nuclei. Since nuclei with small charge variations contribute only weakly to HHG, we separated nuclei with small and large variations for better visibility, as shown in Figure 3c and 3f, respectively. The atomic nuclei in the C_4H_6 molecule are labeled numerically for clarity. From Figure 3c,f, it is evident that the HHG emission mainly originates from electron recollision near nuclei H5, H7, H9, and H10. First, focusing on the emission times marked by the dashed lines, we observe that at these three time points, the charge around H5 and H9 increases, while the charge around H7 and H10 decreases. This indicates that HHG in the y direction is mainly induced by charge recombination near H5 and H9. Based on the above analysis, we confirm that the C_4H_6 molecule can emit high-order harmonics in directions perpendicular to the polarization of a linearly polarized laser field. The harmonic intensities in the y and z directions are very similar, and the emissions originate from the recollision of different groups of electrons near the nuclei.

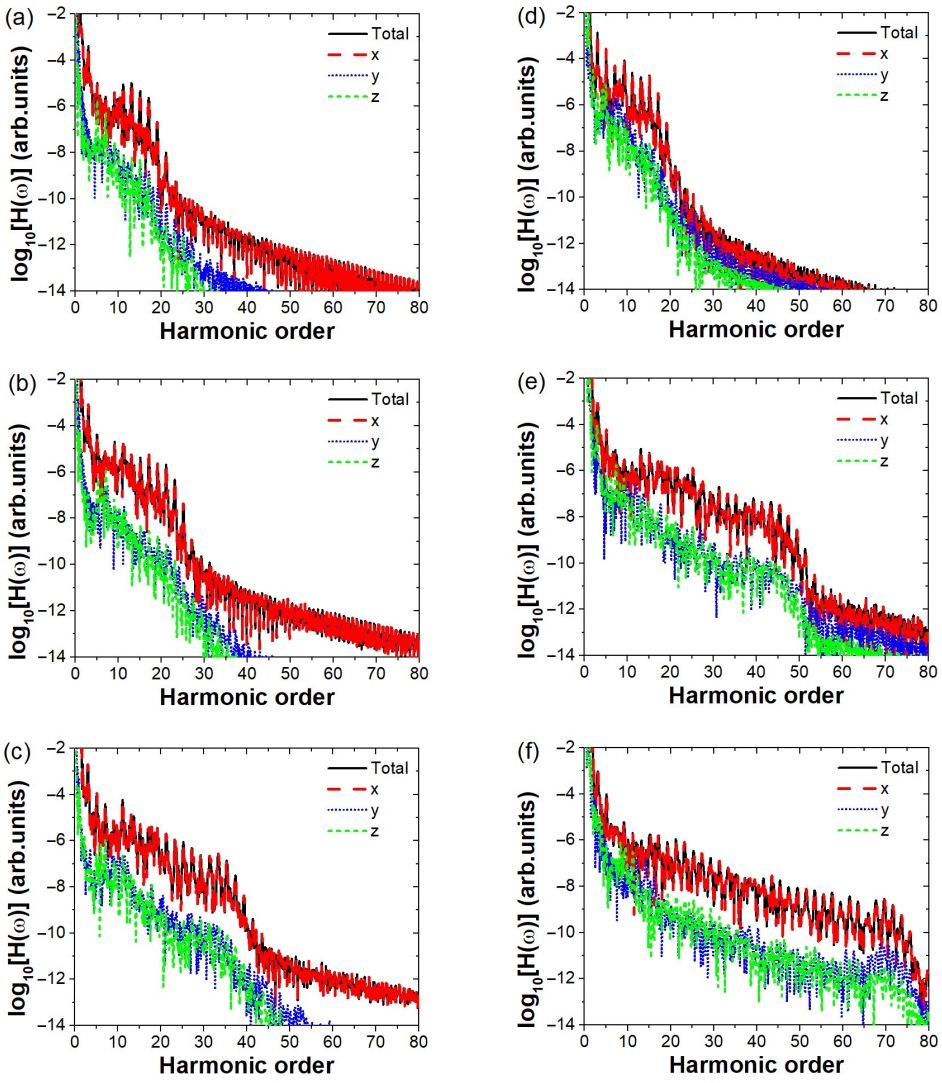

Figure 2. High-harmonic generation of the C_4H_6 molecule under different laser field parameters. (**a**–**c**) Wavelengths of 600 nm, 1000 nm, and 1200 nm, respectively. (**d**–**f**) Field amplitudes of 0.21×10^9 V/cm, 0.26×10^9 V/cm, and 0.36×10^9 V/cm, respectively.

3.2. Synthesis of Circularly Polarized Attosecond Pulses

Using a linearly polarized field with a $\sin^2$ envelope, we obtain a harmonic plateau with a high degree of ellipticity. The harmonic spectrum is shown in Figure 4a. The $\sin^2$ envelope field (Figure 4c) has a wavelength of 800 nm, a total duration of two optical cycles, and a peak amplitude of 0.46×10^9 V/cm, corresponding to approximately 2.84×10^{14} W/cm^2. The polarization direction is along the x-axis, while the molecular axis lies along the z-axis. The blue and green lines represent the harmonic components in the y and z directions, which are comparable in intensity within harmonic orders from 21 to 42. The cyan dashed line represents the degree of ellipticity, which varies within the range of 0.7 to 0.9 within this region. We selected the harmonic orders from 23 to 32 and performed an inverse Fourier transformation to synthesize the attosecond pulse, which is shown in Figure 4b. The resulting attosecond pulse is an isolated elliptically polarized pulse in the x-z plane with a full width at half maximum (FWHM) of approximately 600 as.

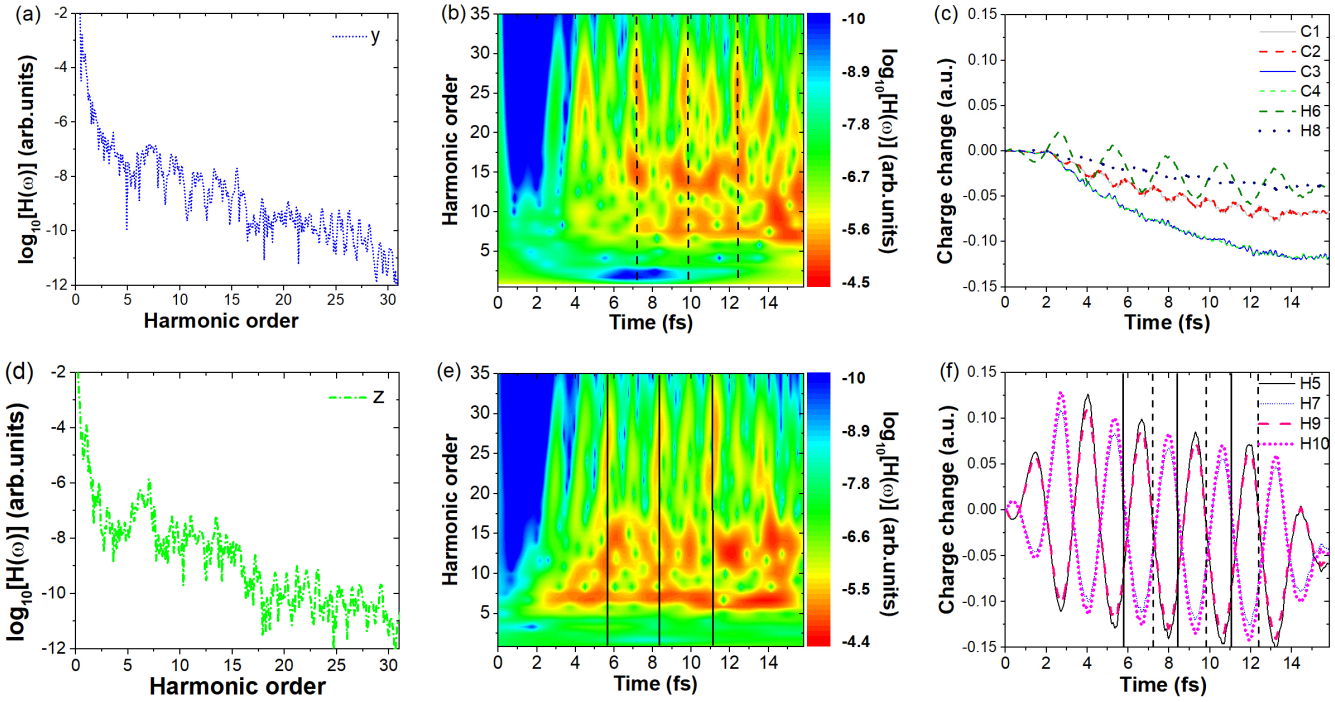

Figure 3. (**a**,**d**) show the high-order harmonic spectra along the *y* and *z* directions from Figure 1a. (**b**,**e**) present the time–frequency analysis of the spectra in (**a**,**d**), where dashed and solid lines indicate the three dominant emission times for the *y* and *z* directions, respectively. (**c**,**f**) display the time-dependent charge variations around different nuclei.

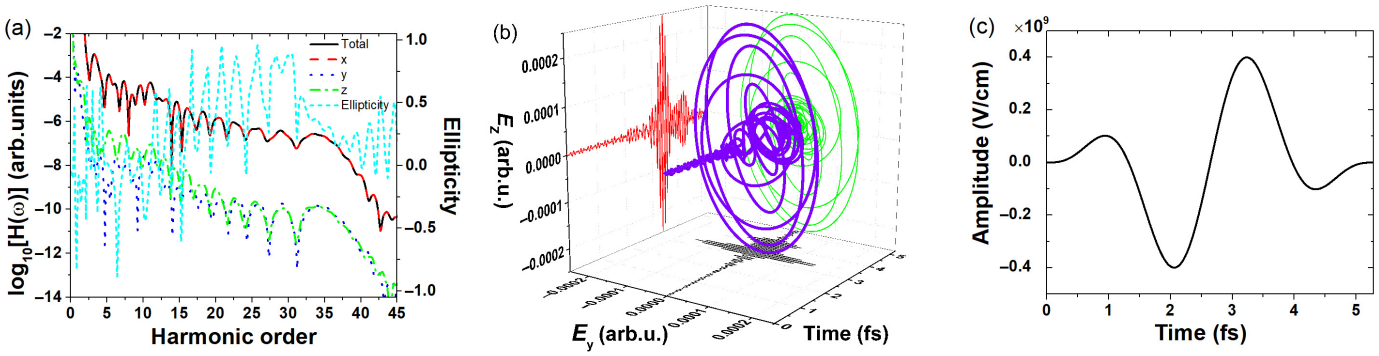

Figure 4. (**a**) The high-order harmonic spectra and ellipticity of the C_4H_6 molecule driven by a linearly polarized laser field with a $\sin^2$ envelope. The black, red, blue, and green curves represent the total harmonic spectrum and the components along the *x*, *y*, and *z* directions, respectively. The cyan curve shows the ellipticity of the harmonics. (**b**) An isolated attosecond pulse (in the figure, the blue curve) synthesized from harmonic orders 23 to 32 in (**a**). The black, red, and green curves represent the projections of the attosecond pulse on different planes. (**c**) An incident laser electric field with a $\sin^2$ envelope polarized along the *x*-direction.

To identify the different orbital contributions to the harmonics in the *y* and *z* directions, we performed an orbital-resolved analysis of the harmonic spectra, and the results are shown in Figure 5. To investigate the contribution of the HOMO to the harmonic generation in the C_4H_6 molecule, we analyzed both the total high-order harmonic spectrum and the spectrum originating from the HOMO. Since the HOMO of C_4H_6 consists of degenerate orbitals, we plotted the ground-state wavefunctions of all relevant orbitals for clarity, as shown in Figure 5e–o. Degenerate orbitals are distinguished by the letters a and b. The Cartesian coordinate system indicates that the observed plane is the *y*-*z* plane. Additionally,

we present the individual harmonic spectra of HOMOa and HOMOb, as well as their combined contribution. The results for the y- and z-polarized components are shown in Figure 5a and 5b, respectively. The green dashed curves represent the total harmonic spectra in each direction. The black solid, red dashed lines, and blue dash–dot lines correspond to the harmonic spectra generated from HOMOa, HOMOb, and the combined contribution of HOMOa and HOMOb, respectively, while the purple dotted lines represent the spectra from a group of dominant orbitals. In Figure 5a, the harmonics of HOMOa and HOMOb exhibit comparable intensities across all orders, with their spectra nearly overlapping. However, while both are close in intensity to the total harmonics in the plateau region (12th–40th orders), they do not fully coincide, especially in the low-order region (below the 12th order). This indicates that these HOMOs do not account for the total harmonic response (which includes contributions from HOMOa to HOMO–7). In contrast, the red dotted line, representing contributions from HOMOa to HOMO–4 (eight orbitals), agrees well with the total spectrum in the plateau region, suggesting that these orbitals are the main contributors to the harmonic emission in the y direction. A similar analysis for Figure 5b reveals that the harmonic emissions in the z direction also primarily originate from the same group of orbitals.

Furthermore, we investigated the reason why the total harmonic spectrum from HOMOa and HOMOb was weaker than those generated from each orbital individually by analyzing the harmonic phases. As shown in Figure 5c,d, below the 30th harmonic order, destructive interference occurs between HOMOa and HOMOb in both the y and z directions due to a phase difference close to π, resulting in a reduced overall intensity. However, above the 30th order, the behavior differs significantly between the two directions: while the y direction maintains a phase difference of approximately π, the phases in the z direction gradually converge, leading to constructive interference and an enhanced total harmonic spectrum compared to those from either orbital alone.

To confirm the respective contributions of the HOMO and the eight dominant molecular orbitals to the harmonic emission, we synthesized attosecond pulses using the 23rd–32nd-order harmonics generated separately from the degenerate HOMO (HOMOa and HOMOb) and from the eight orbitals. The results are shown in Figure 6a–c. From Figure 6, it can be observed that the attosecond pulse synthesized from the HOMO harmonics (Figure 6a,b) does not match the one obtained from the total harmonics. In contrast, the attosecond pulse synthesized from the eight molecular orbitals (Figure 6c) almost completely agrees with that from the total harmonics. This further confirms that these eight orbitals are the main contributors to the harmonic emission in the y and z directions.

Although we obtained an isolated attosecond pulse, its ellipticity was not high, indicating that the pulse was nearly elliptical rather than circularly polarized. To generate a circularly polarized isolated attosecond pulse, it was necessary to adjust the parameters of the incident laser field. We varied the carrier-envelope phase (CEP), and the synthesized attosecond pulses under different CEPs are shown in Figure 7. Figure 7a–f present the attosecond pulses synthesized with CEP values ranging from 30° to 180° in steps of 30°. As shown in Figure 7, the ellipticity of the attosecond pulses varies significantly with the CEP. For example, Figure 7a shows that at a CEP of 30°, the generated attosecond pulse is isolated and nearly circularly polarized. In contrast, the attosecond pulses shown in Figure 7b,c,e,f exhibit elliptical polarization. Additionally, the attosecond pulse shown in Figure 7d is clearly not isolated. These variations suggest that it is possible to manipulate the ellipticity of the synthesized attosecond pulses by adjusting the parameters of the incident laser. By optimizing the wavelength and amplitude of the incident laser field further, more circularly polarized and stronger isolated attosecond pulses may be achievable.

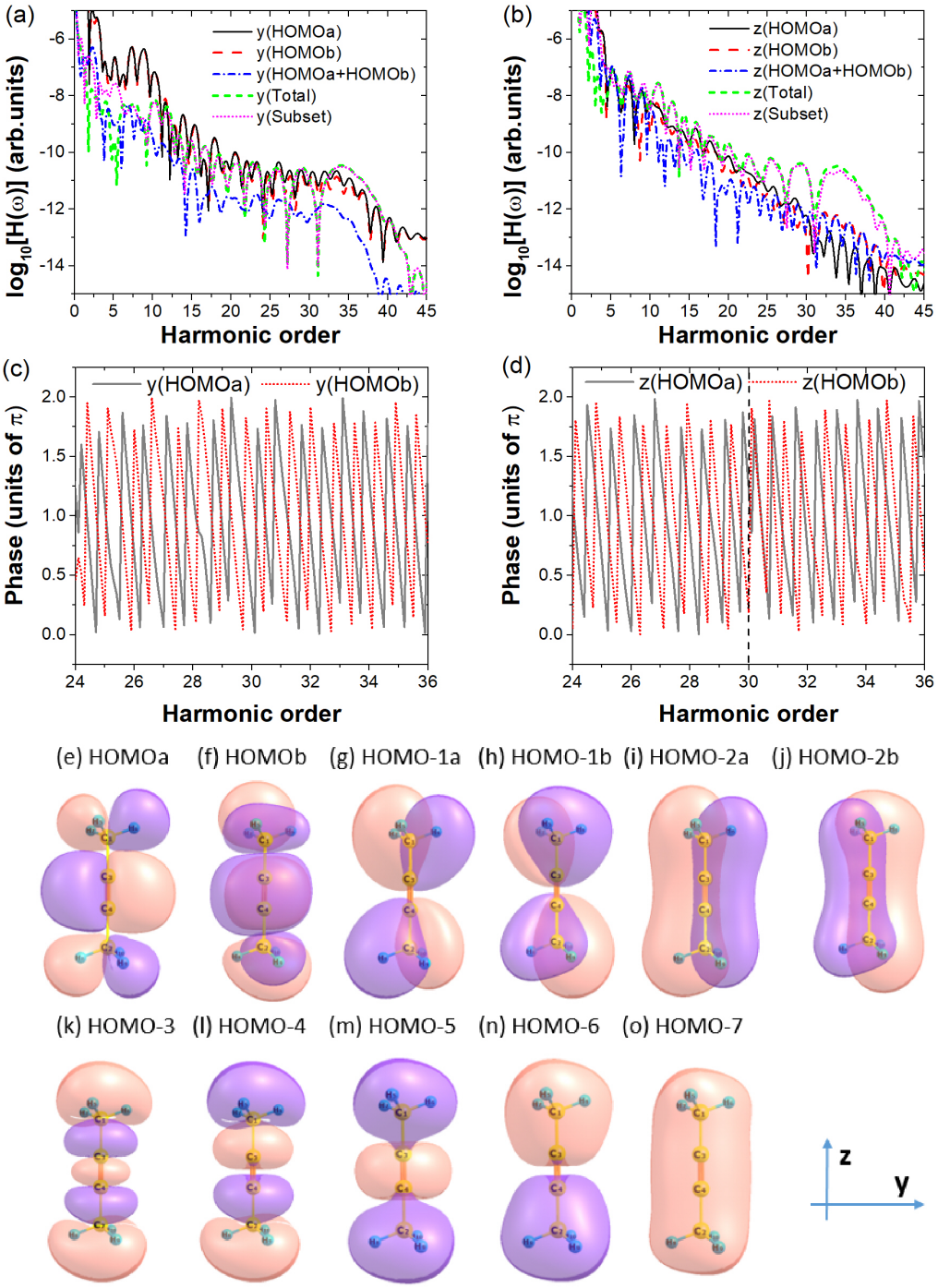

Figure 5. Here, (**a**,**b**) show the high-order harmonic spectra in the *y*- and *z*-directions, respectively. The green short-dashed curves represent the total harmonic spectra in each direction. The black solid and red dashed curves correspond to the harmonic spectra generated by HOMOa and HOMOb, respectively. The blue dash–dotted curve represents the harmonics arising from the combined contributions of HOMOa and HOMOb, while the purple dotted curves depict the spectra originating from a group of dominant orbitals (HOMOa–HOMO-4). (**c**) Harmonic phases of HOMOa and HOMOb along the *y*-direction, from the 24th to 36th orders. (**d**) Harmonic phases of HOMOa and HOMOb along the *z*-direction, from the 24th to 36th orders. The black dashed line marks the 30th order, serving to distinguish the distinct phase characteristics between the 24th–30th and 30th–36th orders. (**e**–**o**) show the molecular orbitals of the C_4H_6 molecule in its ground state. Degenerate orbitals are distinguished by the letters a and b. The Cartesian coordinate system indicates that the observed plane is the *y*-*z* plane.

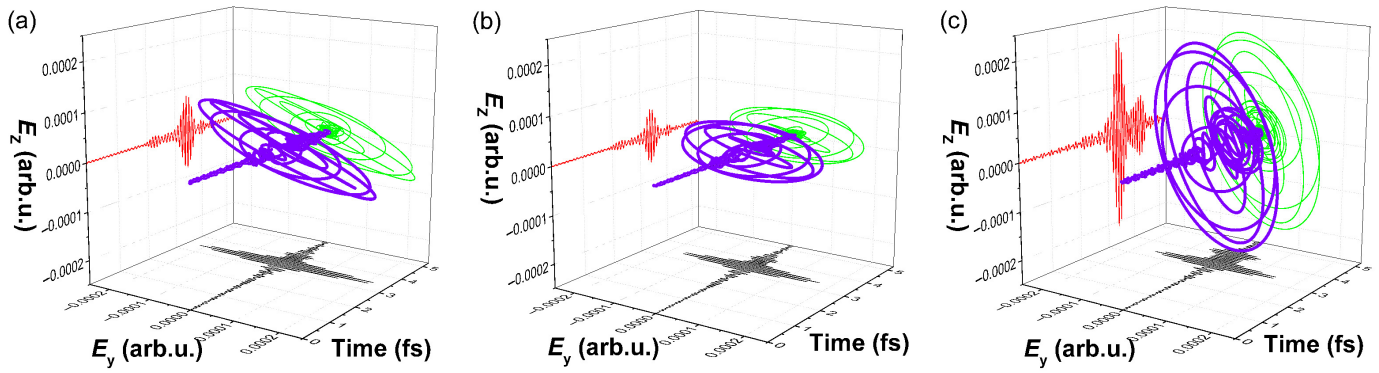

Figure 6. Attosecond pulses (the blue curve) synthesized from the 23rd–32nd order harmonics of (**a**) HOMOa and (**b**) HOMOb. The black, red, and green curves represent the projections of the attosecond pulse on different planes. (**c**) Attosecond pulse synthesized from the 23rd–32nd-order harmonics of the eight dominant molecular orbitals contributing to the harmonic emissions.

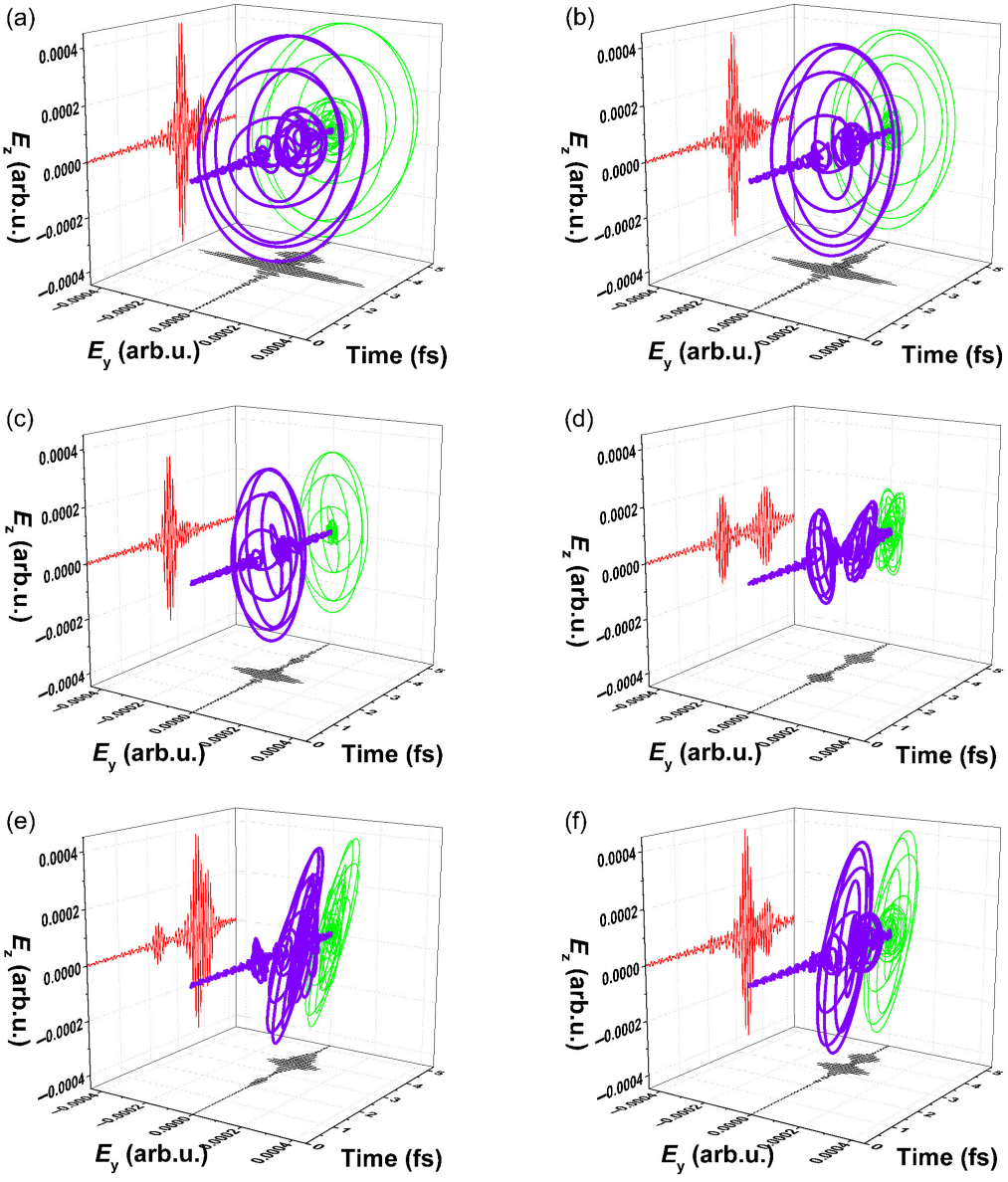

Figure 7. Attosecond pulses (the blue curve) synthesized under different CEPs. The black, red, and green curves represent the projections of the attosecond pulse on different planes. (**a**–**f**) correspond to CEP values ranging from 30° to 180° in steps of 30°.

4. Conclusions

In this work, we investigated the high-order harmonic generation from the C_4H_6 molecule driven by a linearly polarized laser field using time-dependent density functional theory. Remarkably, strong HHG signals were observed not only along the laser polarization direction (x-axis) but also in the directions orthogonal to it (y and z axes). The y- and z-polarized components exhibited typical HHG spectral characteristics, including a clear plateau and cutoff, with intensities about two orders of magnitude lower than those in the x-direction. This orthogonal emission feature is notably distinct from that in reference systems (C_4H_2, C_2H_2, and Be), all of which show negligible HHG emissions in the y and z directions under similar laser parameters.

Further analysis of the time-dependent charge dynamics around individual nuclei, along with a time–frequency analysis, reveals that the y- and z-polarized harmonics originate from different sets of electron recombination events involving distinct hydrogen atoms. These insights suggest that the y and z components are coherent and potentially phase-locked, creating conditions favorable for synthesizing elliptically or even circularly polarized attosecond pulses.

By tailoring the driving laser field using a $\sin^2$ envelope and optimizing the carrier-envelope phase, we successfully synthesized isolated attosecond pulses with high ellipticity in the y-z plane. An orbital-resolved analysis indicates that contributions from multiple orbitals (HOMOa to HOMO-7) are essential for reproducing the total HHG spectrum and generating highly elliptic attosecond bursts. Moreover, by tuning the CEP of the incident pulse, we demonstrated controllable modulation of the polarization state of the generated attosecond pulses, opening a promising route to generating strong and isolated circularly polarized attosecond pulses from achiral molecules under linearly polarized laser fields.

These findings not only deepen our understanding of orthogonal HHG mechanisms in polyatomic molecules but also provide a practical scheme for generating circularly polarized attosecond pulses, which are of great significance for applications in ultrafast spectroscopy and chiral-sensitive light–matter interaction studies.

Author Contributions: Conceptualization: M.H.; methodology: H.W.; software: H.W.; validation: N.X.; formal analysis: N.X.; investigation: D.W.; resources: S.Z.; data curation: S.Z.; writing—original draft preparation: S.Z.; writing—review and editing: N.X.; supervision: M.H. All authors have read and agreed to the published version of the manuscript.

Funding: This research was supported by the National Natural Science Foundation of China (NSFC) under Grant No. 12204214 and the Jilin Provincial Education Department (No. JJKH20230284KJ).

Data Availability Statement: The data presented in this study are available on request from the corresponding author.

Conflicts of Interest: The authors declare no conflicts of interest.

References

1. Strickland, D.; Mourou, G. Compression of amplified chirped optical pulses. *Opt. Commun.* **1985**, *55*, 447–449. [CrossRef]
2. Yanovsky, V.; Chvykov, V.; Kalinchenko, G.; Rousseau, P.; Planchon, T.; Matsuoka, T.; Maksimchuk, A.; Nees, J.; Cheriaux, G.; Mourou, G.; et al. Ultra-high intensity- 300-TW laser at 0.1 Hz repetition rate. *Opt. Express* **2008**, *16*, 2109–2114. [CrossRef]
3. Schenkel, B.; Biegert, J.; Keller, U.; Vozzi, C.; Nisoli, M.; Sansone, G.; Stagira, S.; Silvestri, S.D.; Svelto, O. Generation of 3.8-fs pulses from adaptive compression of a cascaded hollow fiber supercontinuum. *Opt. Lett.* **2003**, *28*, 1987–1989. [CrossRef] [PubMed]
4. Wirth, A.; Hassan, M.T.; Grguraš, I.; Gagnon, J.; Moulet, A.; Luu, T.T.; Pabst, S.; Santra, R.; Alahmed, Z.A.; Azzeer, A.M.; et al. Synthesized Light Transients. *Science* **2011**, *334*, 195–200. [CrossRef]
5. Baltuška, A.; Fuji, T.; Kobayashi, T. Visible pulse compression to 4 fs by optical parametric amplification and programmable dispersion control. *Opt. Lett.* **2002**, *27*, 306–308. [CrossRef]

6. Franken, P.A.; Hill, A.E.; Peters, C.W.; Weinreich, G. Generation of Optical Harmonics. *Phys. Rev. Lett.* **1961**, *7*, 118–119. [CrossRef]
7. Gordon, A.; Kärtner, F.X. Scaling of keV HHG photon yield with drive wavelength. *Opt. Express* **2005**, *13*, 2941–2947. [CrossRef]
8. Qiao, Y.; Zhang, S.; Jiang, W.; Guo, F.; Wang, J.; Chen, J.; Yang, Y. Modulation of harmonics from solids by laser pulses with a small chirp. *Phys. Rev. A* **2025**, *111*, 013501. [CrossRef]
9. Xu, N.; Zhou, S.S.; Wang, Y. Regulation of helium atom higher harmonic emission and attosecond pulse angle in inhomogeneous fields. *Results Phys.* **2025**, *72*, 108190. [CrossRef]
10. Tong, X.M. Multiscale simulation of high-order harmonic generation: From microscopic to macroscopic. *Phys. Rev. A* **2023**, *108*, 023118. [CrossRef]
11. Ding, Z.W.; Wang, Y.B.; Li, Z.L.; Bian, X.B. High-order harmonic generation in liquids in bicircularly polarized laser fields. *Phys. Rev. A* **2023**, *107*, 013503. [CrossRef]
12. Li, M.; Xie, M.F.; Wang, H.; Jia, L.; Li, J.; Wang, W.; Cai, J.; Hong, X.; Shi, X.; Lv, Y.; et al. Observation of Laser-Assisted Dynamic Interference by Attosecond Controlled Photoelectron Spectroscopy. *Phys. Rev. Lett.* **2024**, *133*, 253201. [CrossRef]
13. Chang, Z. Single attosecond pulse and xuv supercontinuum in the high-order harmonic plateau. *Phys. Rev. A* **2004**, *70*, 043802. [CrossRef]
14. Li, J.B.; Zhang, X.; Yue, S.J.; Wu, H.M.; Hu, B.T.; Du, H.C. Enhancement of the second plateau in solid high-order harmonic spectra by the two-color fields. *Opt. Express* **2017**, *25*, 18603–18613. [CrossRef] [PubMed]
15. Yu, C.; Iravani, H.; Madsen, L.B. Crystal-momentum-resolved contributions to multiple plateaus of high-order harmonic generation from band-gap materials. *Phys. Rev. A* **2020**, *102*, 033105. [CrossRef]
16. Corkum, P.B. Plasma perspective on strong field multiphoton ionization. *Phys. Rev. Lett.* **1993**, *71*, 1994–1997. [CrossRef]
17. Gibson, G.; Luk, T.S.; Rhodes, C.K. Tunneling ionization in the multiphoton regime. *Phys. Rev. A* **1990**, *41*, 5049–5052. [CrossRef] [PubMed]
18. Augst, S.; Strickland, D.; Meyerhofer, D.D.; Chin, S.L.; Eberly, J.H. Tunneling ionization of noble gases in a high-intensity laser field. *Phys. Rev. Lett.* **1989**, *63*, 2212–2215. [CrossRef]
19. Sørngård, S.A.; Simonsen, S.I.; Hansen, J.P. High-order harmonic generation from graphene: Strong attosecond pulses with arbitrary polarization. *Phys. Rev. A* **2013**, *87*, 053803. [CrossRef]
20. Lewenstein, M.; Balcou, P.; Ivanov, M.Y.; L'Huillier, A.; Corkum, P.B. Theory of high-harmonic generation by low-frequency laser fields. *Phys. Rev. A* **1994**, *49*, 2117–2132. [CrossRef]
21. Chen, F.; Luo, J.; Luo, F. Single circularly polarized attosecond pulse generation by spatially inhomogeneous fields from atoms with nonvanishing angular quantum number. *Opt. Commun.* **2015**, *342*, 68–72. [CrossRef]
22. Hernández-García, C.; Durfee, C.G.; Hickstein, D.D.; Popmintchev, T.; Meier, A.; Murnane, M.M.; Kapteyn, H.C.; Sola, I.J.; Jaron-Becker, A.; Becker, A. Schemes for generation of isolated attosecond pulses of pure circular polarization. *Phys. Rev. A* **2016**, *93*, 043855. [CrossRef]
23. Bandrauk, A.D.; Guo, J.; Yuan, K.J. Circularly polarized attosecond pulse generation and applications to ultrafast magnetism. *J. Opt.* **2017**, *19*, 124016. [CrossRef]
24. Shao, R.; Zhai, C.; Zhang, Y.; Sun, N.; Cao, W.; Lan, P.; Lu, P. Generation of isolated circularly polarized attosecond pulses by three-color laser field mixing. *Opt. Express* **2020**, *28*, 15874–15884. [CrossRef]
25. Zhong, C.; Qiao, B.; Zhang, Y.; Zhang, Y.; Li, X.; Wang, J.; Zhou, C.; Zhu, S.; He, X. Production of intense isolated attosecond pulses with circular polarization by using counter-propagating relativistic lasers. *New J. Phys.* **2021**, *23*, 063080. [CrossRef]
26. Brooks, N.J.; de las Heras, A.; Wang, B.; Binnie, I.; Serrano, J.; San Román, J.; Plaja, L.; Kapteyn, H.C.; Hernández-García, C.; Murnane, M.M. Circularly Polarized Attosecond Pulses Enabled by an Azimuthal Phase and Polarization Grating. *ACS P hotonics* **2025**, *12*, 495–504. [CrossRef]
27. Svoboda, V.; Waters, M.D.J.; Zindel, D.; Wörner, H.J. Generation and complete polarimetry of ultrashort circularly polarized extreme-ultraviolet pulses. *Opt. Express* **2022**, *30*, 14358–14367. [CrossRef]
28. Han, M.; Ji, J.B.; Ueda, K.; Wörner, H.J. Attosecond metrology in circular polarization. *Optica* **2023**, *10*, 1044–1052. [CrossRef]
29. Chen, S.; Yuan, H.; Wang, F.; Song, J.; Zhao, Y.; Yang, C.; Ou, T.; Zhang, R.; Chang, Q.; Sun, Y. The Generation of Circularly Polarized Isolated Attosecond Pulses with Tunable Helicity from CO Molecules in Polarization Gating Laser Fields. *Photonics* **2024**, *11*, 464. [CrossRef]
30. Sun, N.; Zhu, X.; Wang, B.; Wang, D.; Shao, R.; Lan, P.; Lu, P. Near-circularly-polarized attosecond pulse generation from carbon monoxide molecules with a combination of linearly and circularly polarized fields. *Phys. Rev. A* **2020**, *101*, 053437. [CrossRef]
31. Zhou, S.; Li, Q.; Guo, F.; Wang, J.; Chen, J.; Yang, Y. High-order harmonic generation of benzene molecules irradiated by circularly polarized laser pulses. *Chem. Phys.* **2021**, *545*, 111147. [CrossRef]
32. Pan, C.; Wang, J.; Luan, S.; Zhao, Y.; Leng, Y.; Li, R. Circularly polarized attosecond pulses generation from laser interaction with magnetized sub-critical plasmas. *Plasma Phys. Control. Fusion* **2023**, *65*, 065006. [CrossRef]
33. Zhai, C.; Wu, Y.; Liu, Y.; Zhang, K.; Kang, S.; Li, Z.; Wu, F.; Dong, X.; Cheng, X.; Li, Y.; et al. Near-circularly polarized isolated attosecond pulse generation from gas mixture with two-color multicycle laser fields. *Results Phys.* **2024**, *58*, 107518. [CrossRef]

34. Zhai, C.; Zhu, X.; Li, Y.; Tang, Q.; Yu, B.; Lan, P.; Lu, P. Helicity-selected near-circularly polarized attosecond pulses generated from mixed He-Ne gases. *Phys. Rev. A* **2025**, *111*, 043519. [CrossRef]
35. Tancogne-Dejean, N.; Mücke, O.D.; Kärtner, F.X.; Rubio, A. Impact of the Electronic Band Structure in High-Harmonic Generation Spectra of Solids. *Phys. Rev. Lett.* **2017**, *118*, 087403. [CrossRef]
36. Zhou, S.S.; Yang, Y.J.; Guo, F.M.; Chen, J.G.; Wang, J. Multielectron Effect for High-Order Harmonic Generation From Molecule Irradiated by Bichromatic Counter-Rotating Circularly Polarized Laser Pulses. *IEEE J. Quantum Electron.* **2020**, *56*, 1–7. [CrossRef]
37. Runge, E.; Gross, E.K.U. Density-Functional Theory for Time-Dependent Systems. *Phys. Rev. Lett.* **1984**, *52*, 997–1000. [CrossRef]
38. Perdew, J.P.; Burke, K.; Ernzerhof, M. Generalized Gradient Approximation Made Simple. *Phys. Rev. Lett.* **1996**, *77*, 3865–3868. [CrossRef]
39. Troullier, N.; Martins, J.L. Efficient pseudopotentials for plane-wave calculations. *Phys. Rev. B* **1991**, *43*, 1993–2006. [CrossRef]
40. Kleinman, L.; Bylander, D.M. Efficacious Form for Model Pseudopotentials. *Phys. Rev. Lett.* **1982**, *48*, 1425–1428. [CrossRef]
41. Castro, A.; Marques, M.A.; Rubio, A. Propagators for the time-dependent Kohn-Sham equations. *J. Chem. Phys.* **2004**, *121*, 3425–3433. [CrossRef] [PubMed]
42. Zhou, S.; Wang, H.; Yu, D.; Xu, N.; Hu, M. Enhancing High-Order Harmonic Generation Efficiency Through Molecular Size and Orientation Effects: A Pathway to Ultrafast Chemical Dynamics Studies. *Molecules* **2025**, *30*, 2133. [CrossRef]
43. Zhou, S.; Wang, H.; Hu, M.; Sun, Y.; Zhao, X. Review of the Generation, Regulation, and Applications of High-Order Harmonic Generation in Gases Studied Using Time-Dependent Density Functional Theory. *Symmetry* **2025**, *17*, 359. [CrossRef]
44. Xing, M.; Wang, J.; Zhao, X.; Zhou, S. The Role of Multi-Electron and Multi-Orbital Effects in High-Order Harmonic Generation of Benzonitrile Molecules. *Chin. Phys. Lett.* **2025**, *42*, 043201. [CrossRef]
45. Giovannini, U.D.; Larsen, A.H.; Rubio, A. Modeling electron dynamics coupled to continuum states in finite volumes with absorbing boundaries. *Eur. Phys. J. B* **2015**, *88*, 56. [CrossRef]
46. Burnett, K.; Reed, V.C.; Cooper, J.; Knight, P.L. Calculation of the background emitted during high-harmonic generation. *Phys. Rev. A* **1992**, *45*, 3347–3349. [CrossRef]
47. Milošević, D.B.; Becker, W.; Kopold, R. Generation of circularly polarized high-order harmonics by two-color coplanar field mixing. *Phys. Rev. A* **2000**, *61*, 063403. [CrossRef]
48. Chini, M.; Zhao, K.; Chang, Z. The generation, characterization and applications of broadband isolated attosecond pulses. *Nat. Photonics* **2014**, *8*, 178–186. [CrossRef]
49. Franklin, J.L.; Field, F.H. The Ionization Potentials of Substituted Acetylenes by Electron Impact. *J. Am. Chem. Soc.* **1954**, *76*, 1994–1997. [CrossRef]
50. Schwell, M.; Bénilan, Y.; Fray, N.; Gazeau, M.C.; Es-Sebbar, E.; Gaie-Levrel, F.; Champion, N.; Leach, S. Ionization photophysics and Rydberg spectroscopy of diacetylene. *Mol. Phys.* **2012**, *110*, 2843–2856. [CrossRef]
51. Peter, M.; Daniel, D. High-order harmonic generation from highly excited states in acetylene. *Phys. Rev. A* **2018**, *97*, 043428. [CrossRef]
52. BiÉmont, E.; FrÉmat, Y.; Quinet, P. Ionization Potentials of Atoms and Ions from Lithium to Tin (Z = 50). *At. Data Nucl. Data Tables* **1999**, *71*, 117–146. [CrossRef]
53. Keldysh, L.V. Ionization in the Field of a Strong Electromagnetic Wave. *J. Exp. Theor. Phys.* **1965**, *20*, 1307–1314.